

Active Bayesian Multi-class Mapping from Range and Semantic Segmentation Observations

Arash Asgharivaskasi¹ and Nikolay Atanasov¹

Journal Title
XX(X):1–15
©The Author(s) 2021
Reprints and permission:
sagepub.co.uk/journalsPermissions.nav
DOI: 10.1177/ToBeAssigned
www.sagepub.com/

SAGE

Abstract

The demand for robot exploration in unstructured and unknown environments has recently grown substantially thanks to the host of inexpensive sensing and edge-computing solutions. In order to come closer to full autonomy, robots need to process the measurement stream in real-time, which calls for efficient exploration strategies. Information-based exploration techniques, such as Cauchy-Schwarz quadratic mutual information (CSQMI) and fast Shannon mutual information (FSMI), have successfully achieved active binary occupancy mapping with range measurements. However, as we envision robots performing complex tasks specified with semantically meaningful objects, it is necessary to capture semantic categories in the measurements, map representation, and exploration objective. In this work we propose a Bayesian multi-class mapping algorithm utilizing range-category measurements, as well as a closed-form efficiently computable lower bound for the Shannon mutual information between the multi-class map and the measurements. The bound allows rapid evaluation of many potential robot trajectories for autonomous exploration and mapping. Furthermore, we develop a compressed representation of 3-D environments with semantic labels based on OcTree data structure, where each voxel maintains a categorical distribution over object classes. The proposed 3-D representation facilitates fast computation of Shannon mutual information between the semantic Octomap and the measurements using Run-Length Encoding (RLE) of range-category observation rays. We compare our method against frontier-based and FSMI exploration and apply it in a variety of simulated and real-world experiments.

Keywords

View Planning for SLAM, Reactive and Sensor-Based Planning, Vision-Based Navigation

1 Introduction

Real-time understanding, accurate modeling, and efficient storage of a robot's environment are key capabilities for autonomous operation. Occupancy grid mapping (Elfes 1989; Thrun 2003) is a simple, yet widely used and effective, technique for distinguishing between traversable and occupied 2-D space surrounding a mobile robot. OctoMap technique (Hornung et al. 2013) efficiently expands occupancy grid representation to 3-D environments by compressing similar elements into larger voxels. However, as our vision of delegating increasingly sophisticated tasks to autonomous robots expands, so should the representation power of online mapping algorithms. Augmenting traditional geometric models with semantic information about the context and object-level structure of the environment has become a mainstream problem in robotics (Song et al. 2017; Gan et al. 2020; Wang et al. 2020). Robots are also increasingly expected to operate in unknown environments, with little to no prior information, in applications such as disaster response, environmental monitoring, and reconnaissance. This calls for algorithms allowing robots to autonomously explore unknown environments and construct low-uncertainty metric-semantic maps in real-time, while taking collision and visibility constraints into account.

This paper considers the active metric-semantic mapping problem, requiring a robot to explore and map an unknown environment, relying on streaming distance and object category observations, e.g., generated by semantic

segmentation over RGBD images (Milioto and Stachniss 2019). Our approach extends information-theoretic active mapping techniques (Julian et al. 2013; Charrow et al. 2015; Zhang et al. 2019) from binary to multi-class environment representations. We introduce a Bayesian multi-class mapping procedure which maintains a probability distribution over semantic categories and updates it via a probabilistic range-category perception model. Our main **contribution** is the derivation of a closed-form efficiently computable lower bound for the Shannon mutual information between a multi-class occupancy map and a set of range-category measurements. This lower bound allows rapid evaluation of many potential robot trajectories online to (re-)select one that leads to the best trade-off between uncertainty reduction and efficient exploration of the metric-semantic map. Furthermore, we propose a semantic OctoMap representation of the environment which enables efficient evaluation of the Shannon mutual information in 3-D environments via run-length encoding of range-category observation rays. Unlike traditional class-agnostic exploration methods, our model and information measure

¹University of California San Diego, USA

Corresponding author:

Department of Electrical and Computer Engineering, University of California San Diego, CA 92093, USA.

Email: aasghari@eng.ucsd.edu

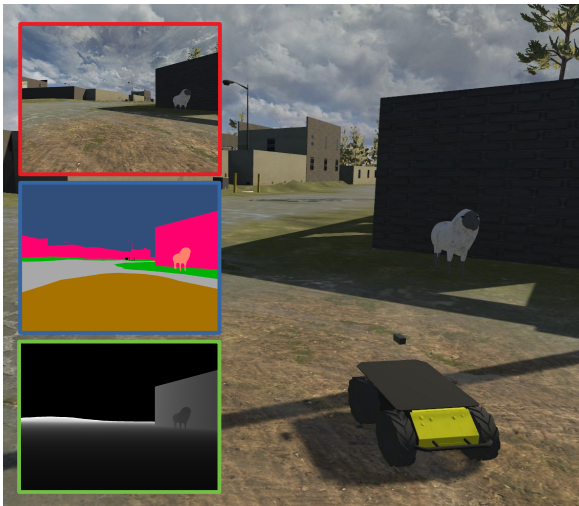


Figure 1. A robot autonomously explores an unknown environment using an RGBD sensor and a semantic segmentation algorithm.

incorporate the uncertainty of different semantic classes, leading to faster and more accurate exploration. The proposed approach relies on general range and class measurements and general motion kinematics, making it suitable for either ground or aerial robots, equipped with either camera or LiDAR sensors, exploring either indoor or outdoor environments.

2 Related Work

Frontier-based exploration (Yamauchi 1997) is a seminal work that highlights the utility of autonomous exploration and active mapping. It inspired methods (Burgard et al. 2005; González-Baños and Latombe 2002) that rely on geometric features, such as the boundaries between free and unknown space (frontiers) and the volume that would be revealed by new sensor observations. Due to their intuitive formulation and low computational requirements, geometry-based methods continue to be widely employed in active perception. Recent works include semantics-assisted indoor exploration (Gómez et al. 2020), active 3D coverage and reconstruction (Cao et al. 2020), and Laplace potential fields for safe outdoor exploration (Maffei et al. 2020). Alternative techniques for active mapping use probabilistic environment models and information-theoretic utility functions to measure and minimize the model uncertainty. The work by Elfes (1995) is among the first to propose an information-based utility function. Information-based exploration strategies have been devised for uncertainty minimization in robot localization or environment mapping (Moorehead et al. 2001; Bourgault et al. 2002; Visser and Slamet 2008). Information-theoretic objectives, however, require integration over the potential sensor measurements, limiting the use of direct numerical approximations to short planning horizons. Kollar and Roy (2008) formulated active mapping using an extended Kalman filter and proposed a local-global optimization, leading to significant gains in efficiency for uncertainty computation and long-horizon planning. Unlike geometry-based approaches, information-theoretic exploration can be directly formulated for active simultaneous localization and

mapping (SLAM) (Carrillo et al. 2012; Carlone et al. 2014; Atanasov et al. 2015; Wang et al. 2019), aiming to determine a sensing trajectory that balances robot state uncertainty and visitation of unexplored map regions. Stachniss et al. (2005) approximate information gain for a Rao-blackwellized particle filter over the joint state of robot pose and map occupancy. Julian et al. (2013) prove that, for range measurements and known robot position, the Shannon mutual information is maximized over trajectories that visit unexplored areas. However, without imposing further structure over the observation model, computing the mutual information objective requires numerical integration. The need for efficient mutual information computation becomes evident in 3-D environments. Cauchy-Schwarz quadratic mutual information (CSQMI) (Charrow et al. 2015) and fast Shannon mutual information (FSMI) (Zhang et al. 2019) offer efficiently computable closed-form objectives for active occupancy mapping with range measurements. Henderson et al. (2020) propose an even faster computation based on a recursive expression for Shannon mutual information in continuous maps. Active semantic mapping has recently attracted much attention due to the proliferation of fast semantic segmentation and object detection algorithms implemented on mobile platforms. Veiga et al. (2021) use a two-layer architecture where the knowledge representation layer provides belief over environment state to the action layer, which subsequently chooses an action to gather information or execute a task. The paper does not specify the semantic mapping method, or type of perception input used to build the semantic mapping. Suriani et al. (2021) present a semantic exploration policy which takes an occluded semantic point cloud of an object, finds a match in a database to estimate the full object dimensions, and then generates candidate next observation poses to reconstruct the object. The next best view is computed via a volumetric information gain metric that computes visible entropy from a candidate pose. The problem with visible entropy is that, unlike Shannon mutual information between the map and a sensor observation, it does not model sensor noise specifications such as range or classification error. Moreover, the semantic map used in this paper is simply a collection of bounding boxes around objects. Active semantic mapping has also been employed to develop sample-efficient deep learning methods. Blum et al. (2019) proposes an active learning method for training semantic segmentation networks where novelty (epistemic uncertainty) of input images is estimated via distance from the training data in the space of the embeddings, while a path planning method maximizes novelty of future input images along the planned trajectory, assuming novel images are spatially correlated. Georgakis et al. (2021) actively train a hierarchical semantic map generation model that predicts occupancy and semantic classes given occluded input. The authors use an ensemble of map generation models in order to predict epistemic uncertainty of the predicted map. The uncertainty is then used to choose trajectories for actively training the model with new images that differ the most with the training data of the current model. Our proposed active semantic mapping method distinguishes itself from the aforementioned works by introducing a dense Bayesian multi-class mapping with a

closed-form uncertainty measure, as opposed to sampling-based uncertainty estimation. Moreover, our information-theoretic objective function directly models sensor noise specifications, unlike volumetric information gain metrics.

This paper is most related to CSQMI (Charrow et al. 2015) and FSMI (Zhang et al. 2019) in that it develops a closed-form expression for mutual information. However, instead of a binary map and range-only measurements, our formulation considers a multi-class map with Bayesian updates from range-category measurements. Since transforming a multi-class map to an occupancy map is a many-to-one relationship, the information associated with various object classes will fail to be captured if we solely rely on occupancy information, as the case in CSQMI and FSMI. Therefore, we expect to perform exploration more efficiently by utilizing the multi-class perception model, and consequently, expanding the concept of uncertainty to multiple classes.

3 Problem Statement

Consider a robot with pose $\mathbf{X}_t \in SE(3)$ at time t and deterministic discrete-time kinematics:

$$\mathbf{X}_t := \begin{bmatrix} \mathbf{R}_t & \mathbf{p}_t \\ \mathbf{0}^\top & 1 \end{bmatrix}, \quad \mathbf{X}_{t+1} = \mathbf{X}_t \exp(\hat{\mathbf{u}}_t), \quad (1)$$

where $\mathbf{R}_t \in SO(3)$ is the robot orientation, $\mathbf{p}_t \in \mathbb{R}^3$ is the robot position, and $\mathbf{u}_t := [\mathbf{v}_t^\top, \boldsymbol{\omega}_t^\top]^\top \in \mathcal{U} \subset \mathbb{R}^6$ is the control input, consisting of linear velocity $\mathbf{v}_t \in \mathbb{R}^3$ and angular velocity $\boldsymbol{\omega}_t \in \mathbb{R}^3$. The function $(\cdot) : \mathbb{R}^6 \rightarrow \mathfrak{se}(3)$ maps vectors in \mathbb{R}^6 to the Lie algebra $\mathfrak{se}(3)$. The robot is navigating in an environment represented as a collection of disjoint sets $\mathcal{E}_k \subset \mathbb{R}^3$, each associated with a semantic category $k \in \mathcal{K} := \{0, 1, \dots, K\}$. Let \mathcal{E}_0 denote free space, while each \mathcal{E}_k for $k > 0$ represents a different category, such as buildings, animals, terrain (see Fig. 1).

We assume that the robot is equipped with a sensor that provides information about the distance to and semantic categories of surrounding objects along a set of rays $\mathcal{F} := \{\eta_b\}_b$, where b is the ray index, $\eta_b \in \mathbb{R}^3$ with $\|\eta_b\|_2 = r_{max}$, and $r_{max} > 0$ is the maximum sensing range.

Definition 1. A *sensor observation* at time t from robot pose \mathbf{X}_t is a collection $\mathcal{Z}_t := \{\mathbf{z}_{t,b}\}_b$ of range and category measurements $\mathbf{z}_{t,b} := (r_{t,b}, y_{t,b}) \in \mathbb{R}_{\geq 0} \times \mathcal{K}$, acquired along the sensor rays $\mathbf{R}_t \eta_b$ with $\eta_b \in \mathcal{F}$ at robot position \mathbf{p}_t .

Such information may be obtained by processing the observations of an RGBD camera or a Lidar with a semantic segmentation algorithm (Milioto and Stachniss 2019). The goal is to construct a multi-class map \mathbf{m} of the environment based on the labeled range measurements. We model \mathbf{m} as a grid of cells m_i , $i \in \mathcal{I} := \{1, \dots, N\}$, each labeled with a category $m_i \in \mathcal{K}$. In order to model noisy sensor observations, we consider a probability density function (PDF) $p(\mathcal{Z}_t | \mathbf{m}, \mathbf{X}_t)$. This observation model allows integrating the measurements into a probabilistic map representation using Bayesian updates. Let $p_t(\mathbf{m}) := p(\mathbf{m} | \mathcal{Z}_{1:t}, \mathbf{X}_{1:t})$ be the probability mass function (PMF) of the map \mathbf{m} given the robot trajectory $\mathbf{X}_{1:t}$ and observations $\mathcal{Z}_{1:t}$ up to time t . Given a new observation \mathcal{Z}_{t+1} obtained from robot pose \mathbf{X}_{t+1} , the Bayesian update to the map PMF is:

$$p_{t+1}(\mathbf{m}) \propto p(\mathcal{Z}_{t+1} | \mathbf{m}, \mathbf{X}_{t+1}) p_t(\mathbf{m}). \quad (2)$$

We assume that the robot pose is known and omit the dependence of the map distribution and the observation model on it for brevity. We consider the following problem.

Problem Given a prior map PMF $p_t(\mathbf{m})$ and a finite planning horizon T , find a control sequence $\mathbf{u}_{t:t+T-1}$ for the model in (1) that maximizes the ratio of mutual information $I(\mathbf{m}; \mathcal{Z}_{t+1:t+T} | \mathcal{Z}_{1:t})$ between the map \mathbf{m} and future sensor observations $\mathcal{Z}_{t+1:t+T}$ and the motion cost $J(\mathbf{X}_{t:t+T-1}, \mathbf{u}_{t:t+T-1})$ of the planned robot trajectory:

$$\max_{\mathbf{u}_{t:t+T-1}} \frac{I(\mathbf{m}; \mathcal{Z}_{t+1:t+T} | \mathcal{Z}_{1:t})}{J(\mathbf{X}_{t:t+T-1}, \mathbf{u}_{t:t+T-1})} \text{ subject to (1), (2).} \quad (3)$$

The precise definitions of the mutual information and motion cost terms above are:

$$I(\mathbf{m}; \mathcal{Z}_{t+1:t+T} | \mathcal{Z}_{1:t}) := \sum_{\mathbf{m} \in \mathcal{K}^N} \int \dots \int p(\mathbf{m}, \mathcal{Z}_{t+1:t+T} | \mathcal{Z}_{1:t})$$

$$\times \log \frac{p(\mathbf{m}, \mathcal{Z}_{t+1:t+T} | \mathcal{Z}_{1:t})}{p(\mathbf{m} | \mathcal{Z}_{1:t}) p(\mathcal{Z}_{t+1:t+T} | \mathcal{Z}_{1:t})} \prod_{\tau=1}^T \prod_b d\mathbf{z}_{t+\tau,b} \quad (4)$$

$$J(\mathbf{X}_{t:t+T-1}, \mathbf{u}_{t:t+T-1}) := q(\mathbf{X}_{t+T}) + \sum_{\tau=0}^{T-1} c(\mathbf{X}_{t+\tau}, \mathbf{u}_{t+\tau}),$$

where $q(\mathbf{X})$, $c(\mathbf{X}, \mathbf{u}) > 0$ model terminal and stage motion costs (e.g., distance traveled, elapsed time), respectively.

We develop a multi-class extension to the log-odds occupancy mapping algorithm (Thrun et al. 2005, Ch. 9) in Sec. 4 and derive an efficient approximation to the mutual information term in Sec. 5. In Sec. 6 we present multi-class Shannon mutual information over a semantic Octomap, which is a multi-class extension of the OctoMap (Hornung et al. 2013) technique. This allows us to autonomously explore large 3-D environments via evaluating potential robot trajectories online and (re-)select the one that maximizes the objective in (3), leading to efficient active multi-class 3-D mapping. Finally in Sec. 7, we demonstrate the performance of the proposed work in a variety of simulated and real-world experiments.

4 Bayesian Multi-class Mapping

This section derives the Bayesian update in (2), using a *multinomial logit model* to represent $p_t(\mathbf{m})$. To ensure that the number of parameters in the model scales linearly with the map size N , we maintain a factorized PDF over the cells:

$$p_t(\mathbf{m}) = \prod_{i=1}^N p_t(m_i). \quad (5)$$

We represent the individual cell PDFs $p_t(m_i)$ over \mathcal{K} using a vector of log odds:

$$\mathbf{h}_{t,i} := \left[\log \frac{p_t(m_i=0)}{p_t(m_i=0)} \quad \dots \quad \log \frac{p_t(m_i=K)}{p_t(m_i=0)} \right]^\top \in \mathbb{R}^{K+1}, \quad (6)$$

where the free-class likelihood $p_t(m_i=0)$ is used as a pivot. Given the log-odds vector $\mathbf{h}_{t,i}$, the PDF of cell m_i may be recovered using the softmax function $\sigma : \mathbb{R}^{K+1} \mapsto \mathbb{R}^{K+1}$:

$$p_t(m_i = k) = \sigma_{k+1}(\mathbf{h}_{t,i}) := \frac{\mathbf{e}_{k+1}^\top \exp(\mathbf{h}_{t,i})}{\mathbf{1}^\top \exp(\mathbf{h}_{t,i})}, \quad (7)$$

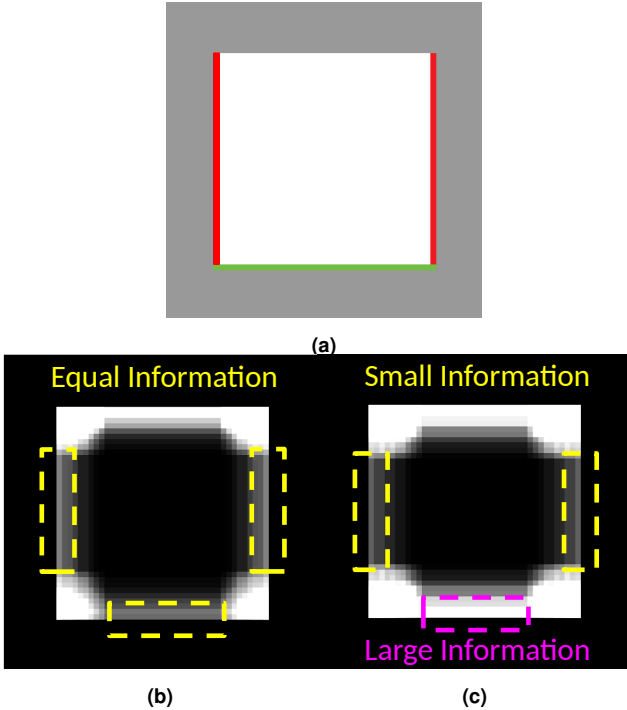


Figure 2. Comparison of information surfaces between the proposed method and FSMI. (a) Test environment with classes *free*, *class*₁, and *class*₂ where the white and gray regions represent free and unknown spaces, respectively, and the red and green walls have the same occupancy probability with different uncertainty among object classes. (b) Occupancy mutual information surface computed from FSMI. (c) Semantic mutual information surface computed using the proposed Bayesian multi-class mapping. The mutual information is shown proportional to pixel brightness.

where \mathbf{e}_k is the standard basis vector with k -th element equal to 1 and 0 elsewhere, and $\mathbf{1}$ is the vector with all elements equal to 1. To derive Bayes rule for the log-odds $\mathbf{h}_{t,i}$, we need to specify an observation model for the measurements.

Definition 2. The *inverse observation model* of a range-category measurement \mathbf{z} obtained from robot pose \mathbf{X} along sensor ray $\boldsymbol{\eta} \in \mathcal{F}$ with respect to map cell m_i is a probability density function $p(m_i = k | \mathbf{z}; \mathbf{X}, \boldsymbol{\eta})$.

The Bayesian update in (2) for $\mathbf{h}_{t,i}$ can be obtained in terms of the range-category inverse observation model, evaluated at the new measurement set \mathcal{Z}_{t+1} .

Proposition 1. Let $\mathbf{h}_{t,i}$ be the log odds of cell m_i at time t . Given sensor observation \mathcal{Z}_{t+1} , the posterior log-odds are:

$$\mathbf{h}_{t+1,i} = \mathbf{h}_{t,i} + \sum_{\mathbf{z} \in \mathcal{Z}_{t+1}} (\mathbf{l}_i(\mathbf{z}) - \mathbf{h}_{0,i}) \quad (8)$$

where $\mathbf{l}_i(\mathbf{z})$ is the inverse observation model log odds:

$$\mathbf{l}_i(\mathbf{z}) := \begin{bmatrix} \log \frac{p(m_i=0|\mathbf{z})}{p(m_i=1|\mathbf{z})} & \dots & \log \frac{p(m_i=K|\mathbf{z})}{p(m_i=1|\mathbf{z})} \end{bmatrix}^\top. \quad (9)$$

Proof. See Appendix A.

To complete the Bayesian multi-class mapping algorithm suggested by (8) we need a particular inverse observation model. When a sensor measurement is generated, the sensor ray continues to travel until it hits an obstacle of category $\mathcal{K} \setminus \{0\}$ or reaches the maximum sensing range r_{max} . The

resulting labeled range measurement $\mathbf{z} = (r, y)$ indicates that map cell m_i is occupied if the measurement end point $\mathbf{p} + \frac{r}{r_{max}} \mathbf{R} \boldsymbol{\eta}$ lies in the cell. If m_i lies along the sensor ray but does not contain the end point, it is observed as free. Finally, if m_i is not intersected by the sensor ray, no information is provided about its occupancy. The map cells along the sensor ray can be determined by a rasterization algorithm, such as Bresenham's line algorithm (Bresenham 1965). We parameterize the inverse observation model log-odds vector as:

$$\mathbf{l}_i((r, y)) := \begin{cases} \phi^+ + \mathbf{E}_{y+1} \psi^+, & r \text{ indicates } m_i \text{ is occupied,} \\ \phi^-, & r \text{ indicates } m_i \text{ is free,} \\ \mathbf{h}_{0,i}, & \text{otherwise,} \end{cases} \quad (10)$$

where $\mathbf{E}_k := \mathbf{e}_k \mathbf{e}_k^\top$ and $\psi^+, \phi^-, \phi^+ \in \mathbb{R}^{K+1}$ are parameter vectors, whose first element is 0 to ensure that $\mathbf{l}_i(\mathbf{z})$ is a valid log-odds vector. This parameterization leads to inverse observation model $p(m_i = k | \mathbf{z}) = \sigma_{k+1}(\mathbf{l}_i(\mathbf{z}))$, which is piece-wise constant along the sensor ray.

To compute the mutual information between an observation sequence $\mathcal{Z}_{t+1:t+T}$ and the map \mathbf{m} in the next section, we will also need the PDF of a range-category measurement $\mathbf{z}_{\tau,b} \in \mathcal{Z}_{t+1:t+T}$ conditioned on $\mathcal{Z}_{1:t}$. Let $\mathcal{R}_{\tau,b}(r) \subset \mathcal{I}$ denote the set of map cell indices along the ray $\mathbf{R}_\tau \boldsymbol{\eta}_b$ from the robot position \mathbf{p}_τ with length r . Let $\gamma_{\tau,b}(i)$ denote the distance traveled by the ray $\mathbf{R}_\tau \boldsymbol{\eta}_b$ within cell m_i and $i_{\tau,b}^* \in \mathcal{R}_{\tau,b}(r)$ denote the index of the cell hit by $\mathbf{z}_{\tau,b}$. We define the PDF of $\mathbf{z}_{\tau,b} = (r, y)$ conditioned on $\mathcal{Z}_{1:t}$ as:

$$p(\mathbf{z}_{\tau,b} | \mathcal{Z}_{1:t}) = \frac{p_t(m_{i_{\tau,b}^*} = y)}{\gamma_{\tau,b}(i_{\tau,b}^*)} \prod_{i \in \mathcal{R}_{\tau,b}(r) \setminus \{i_{\tau,b}^*\}} p_t(m_i = 0). \quad (11)$$

This definition states that the likelihood of $\mathbf{z}_{\tau,b} = (r, y)$ at time t depends on the likelihood that the cells m_i along the ray $\mathbf{R}_\tau \boldsymbol{\eta}_b$ of length r are empty and the likelihood that the hit cell $m_{i_{\tau,b}^*}$ has class y . A similar model for binary observations has been used in Julian et al. (2013), Charrow et al. (2015), and Zhang et al. (2019).

Prop. 1 provides a probabilistic basis to expand the occupancy grid representation to a multi-class description of the environment, where the Shannon entropy $H[m_i | \mathcal{Z}_{1:t}]$ of a map cell depends on the probability of each class $p_t(m_i = k)$, instead of only the occupancy probability $1 - p_t(m_i = 0)$. Moreover, the inverse observation model of (10) can contain a different probability of detection for each class which can be used to prioritize exploration among different classes. Fig. 2 (a) illustrates an example where the estimated map of an environment with 3 classes of *free*, *class*₁, *class*₂ contains two regions with similar occupancy probability but different semantic uncertainty. In particular, the white region represents free space with probabilities $\mathbf{p}^{white}(m_i) = [1, 0, 0]$, the gray region is unexplored hence $\mathbf{p}^{gray}(m_i) = [0.3, 0.3, 0.3]$, and the red and green regions have the same occupancy probability of $p(m_i = \text{occupied}) = 0.9$ while the red region more certainly belongs to *class*₁ with $\mathbf{p}^{red}(m_i) = [0.1, 0.8, 0.1]$ and the green region has high uncertainty among object classes with $\mathbf{p}^{green}(m_i) = [0.1, 0.45, 0.45]$. As can be seen in Fig. 2 (b), an information metric like the binary mutual information used in FSMI

cannot distinguish between the red and green regions since they both have the same occupancy probability. However, our proposed multi-class mapping takes into account the semantic uncertainty among different object classes; as can be seen in Fig. 2 (c) where the uncertain green region has larger mutual information than the high-certainty red region. Such observations hint the possibility of reaching a more accurate exploration using a multi-class perception model instead of occupancy mapping.

This section focused on how an observation affects the map PDF $p_t(\mathbf{m})$, we now switch our focus to computing of the mutual information between a sequence of observations $\mathcal{Z}_{t+1:t+T}$ and the multi-class occupancy map \mathbf{m} .

5 Informative Planning

Computing the mutual information term in (4) is challenging because it involves integration over all possible values of the observation sequence $\mathcal{Z}_{t+1:t+T}$. Our main result is an efficiently computable lower bound on $I(\mathbf{m}; \mathcal{Z}_{t+1:t+T} | \mathcal{Z}_{1:t})$ for range-category observations $\mathcal{Z}_{t+1:t+T}$ and a multi-class occupancy map \mathbf{m} . The result is obtained by selecting a subset $\underline{\mathcal{Z}}_{t+1:t+T} = \{\mathbf{z}_{\tau,b}\}_{\tau=t+1, b=1}^{t+T, B}$ of the observations $\mathcal{Z}_{t+1:t+T}$ in which the sensor rays are non-overlapping. Precisely, any pair of measurements $\mathbf{z}_{\tau,b}, \mathbf{z}_{\tau',b'} \in \underline{\mathcal{Z}}_{t+1:t+T}$ satisfies:

$$\mathcal{R}_{\tau,b}(r_{max}) \cap \mathcal{R}_{\tau',b'}(r_{max}) = \emptyset. \quad (12)$$

In practice, constructing $\underline{\mathcal{Z}}_{t+1:t+T}$ requires removing intersecting rays from $\mathcal{Z}_{t+1:t+T}$ to ensure that the remaining observations are mutually independent. Consequently, the mutual information between \mathbf{m} and $\underline{\mathcal{Z}}_{t+1:t+T}$ can be obtained as a sum of mutual information terms between single rays $\mathbf{z}_{\tau,b} \in \underline{\mathcal{Z}}_{t+1:t+T}$ and map cells m_i observed by $\mathbf{z}_{\tau,b}$. This idea is inspired by CSQMI (Charrow et al. 2015) but we generalize their results to multi-class observations and map.

Proposition 2. *Given a sequence of labeled range observations $\mathcal{Z}_{t+1:t+T}$, let $\underline{\mathcal{Z}}_{t+1:t+T} = \{\mathbf{z}_{\tau,b}\}_{\tau=t+1, b=1}^{t+T, B}$ be a subset of non-overlapping measurements that satisfy (12). Then, the Shannon mutual information between $\mathcal{Z}_{t+1:t+T}$ and a multi-class occupancy map \mathbf{m} can be lower bounded as:*

$$\begin{aligned} I(\mathbf{m}; \mathcal{Z}_{t+1:t+T} | \mathcal{Z}_{1:t}) &\geq I(\mathbf{m}; \underline{\mathcal{Z}}_{t+1:t+T} | \mathcal{Z}_{1:t}) \\ &= \sum_{\tau=t+1}^{t+T} \sum_{b=1}^B \sum_{k=1}^K \sum_{n=1}^{N_{\tau,b}} p_{\tau,b}(n, k) C_{\tau,b}(n, k), \end{aligned} \quad (13)$$

where $N_{\tau,b} := |\mathcal{R}_{\tau,b}(r_{max})|$,

$$\begin{aligned} p_{\tau,b}(n, k) &:= p_t(m_{i_{\tau,b}^*} = k) \prod_{i \in \mathcal{R}_{\tau,b}(n) \setminus \{i_{\tau,b}^*\}} p_t(m_i = 0), \\ C_{\tau,b}(n, k) &:= f(\phi^+ + \mathbf{E}_{k+1} \psi^+ - \mathbf{h}_{0,i_{\tau,b}^*}, \mathbf{h}_{t,i_{\tau,b}^*}) \\ &\quad + \sum_{i \in \mathcal{R}_{\tau,b}(n) \setminus \{i_{\tau,b}^*\}} f(\phi^- - \mathbf{h}_{0,i}, \mathbf{h}_{t,i}), \\ f(\phi, \mathbf{h}) &:= \log \left(\frac{\mathbf{1}^\top \exp(\mathbf{h})}{\mathbf{1}^\top \exp(\phi + \mathbf{h})} \right) + \phi^\top \sigma(\phi + \mathbf{h}), \end{aligned}$$

Algorithm 1 Information-theoretic Path Planning

Input: $\mathbf{X}_t, p_t(\mathbf{m})$

- 1: $\mathcal{F} = \text{FINDFRONTIERS}(p_t(\mathbf{m}))$
- 2: **for** $f \in \mathcal{F}$ **do**
- 3: $\mathbf{X}_{t+1:t+T}, \mathbf{u}_{t:t+T-1} = \text{PLANPATH}(\mathbf{X}_t, p_t(\mathbf{m}), f)$
- 4: Compute (3) over $\mathbf{X}_{t:t+T}, \mathbf{u}_{t:t+T-1}$ via Prop. (2)
- 5: **return** $\mathbf{X}_{t:t+T}^*, \mathbf{u}_{t:t+T-1}^*$ with highest value

and $\tilde{\mathcal{R}}_{\tau,b}(n) \subseteq \mathcal{R}_{\tau,b}(r_{max})$ is the set of the first n map cell indices along the ray $\mathbf{R}_\tau \eta_b$, i.e., $\tilde{\mathcal{R}}_{\tau,b}(n) := \{i \mid i \in \mathcal{R}_{\tau,b}(r), |\mathcal{R}_{\tau,b}(r)| = n, r \leq r_{max}\}$.

Proof. See Appendix B.

Prop. 2 allows evaluating the informativeness according to (3) of any potential robot trajectory $\mathbf{X}_{t:t+T}, \mathbf{u}_{t:t+T-1}$. We use a motion planning algorithm to obtain a set of trajectories to the map frontiers, determined from the current map PDF $p_t(\mathbf{m})$. Alg. 1 summarizes the procedure for determining a state-control trajectory $\mathbf{X}_{t:t+T}^*, \mathbf{u}_{t:t+T-1}^*$ that maximizes the objective in (3), where $J(\mathbf{X}_{t:t+T-1}, \mathbf{u}_{t:t+T-1})$ is the length of the corresponding path. This kinematically feasible trajectory can be tracked by a low-level controller that takes the robot dynamics into account. We evaluate the proposed active multi-class mapping algorithm in Sec. 7.

6 Information Computation for Semantic OctoMap Representation

Full grid representation of 3D environments demands for expensive processing power and large memory requirements. However, the occupied space in realistic situations is usually distributed sparsely across the environment; while the free space comprises a large and continuous portion of the scene. The OctoMap (Hornung et al. 2013) technique exploits this property in order to provide an efficient variable-sized grid representation of a 3D environment. The OctoMap method combines many small cells associated with the free space into one large cell using an octree data structure; leading to significant gains in terms of memory usage and computational cost. In the following, we first provide a semantic version of the OctoMap technique. Next, we propose an efficient semantic mutual information formula which benefits from the structure of an OctoMap representation.

6.1 Semantic OctoMap

A semantic octree is a hierarchical data structure containing nodes that represent a section of the physical environment. Each node has either 0 or 8 children, where the latter corresponds to the 8 octants of the Euclidean 3-D coordinate system. Therefore, children of a node form a partition of the space which the parent node corresponds to. Fig. 3a illustrates an example of semantic octree data structure. A white circle represents an *inner* node such that its children collectively cover the same physical space as the inner node itself. A Colored square represents a partition of the 3-D space where all downstream nodes contain identical semantic and occupancy values; therefore, they can be *pruned* into a *leaf* node. Lastly, black dots represent *unexplored* spaces of

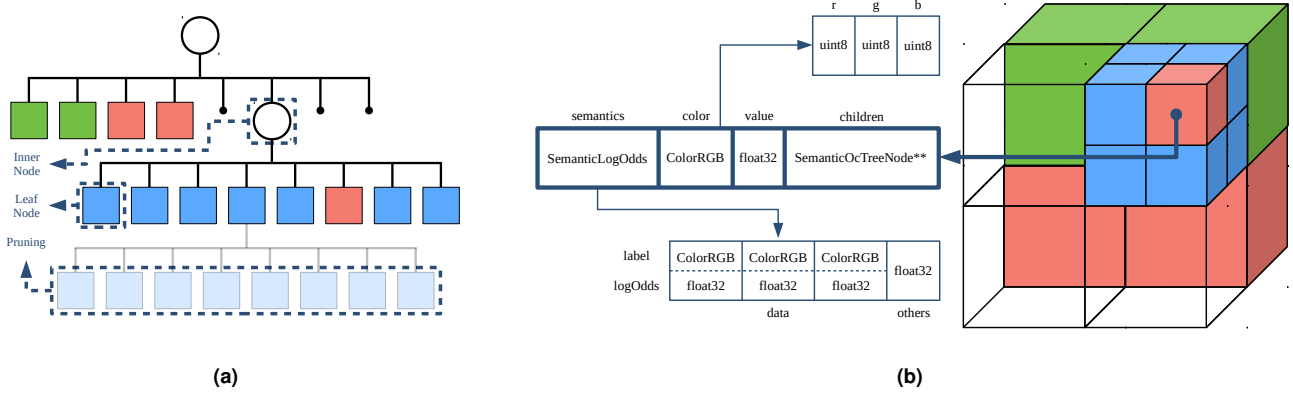


Figure 3. Example of a semantic OctoMap. (a) Octree Data structure with examples of inner nodes, leaf nodes, and pruned nodes. (b) Geometric representation of the same octree with a breakdown of *SemanticOcTreeNode* class.

the environment. Fig. 3b shows the geometric representation of the semantic octree of Fig. 3a.

As the building block of our semantic octree structure, we implement *SemanticOcTreeNode* class which efficiently stores occupancy, color, and semantic information of its corresponding physical space, shown in Fig. 3b. The most important data members of *SemanticOcTreeNode* class are as follows:

- *children*: An array of pointers of *SemanticOcTreeNode* which stores the memory addresses of the 8 child nodes.
- *value*: A *float32* variable storing the occupancy probability of the corresponding node in terms of log-odds ratio.
- *color*: A *ColorRGB* object storing the actual RGB color of the node.
- *semantics*: A *SemanticLogOdds* object which maintains a categorical probability distribution over semantic labels in form of log-odds ratio.

For performance considerations, *SemanticLogOdds* class only stores the multi-class log-odds for the 3 most likely object labels, with each label represented by a unique RGB color. In this case, the log-odds associated with the rest of the labels lump into a single *others* variable. This relieves the semantic octree implementation from dependence on the number of labels that the object classifier can detect. Moreover, it significantly helps to improve the performance of the mapping algorithm in cases where there is a large variety of object labels.

The implementation of semantic octree becomes complete by defining *SemanticOcTree* class; which is derived from *OccupancyOcTreeBase* class of the OctoMap library* and uses *SemanticOcTreeNode* as its node type. Fig. 4 illustrates the derivation of *SemanticOcTree* and *SemanticOcTreeNode* classes in form of a UML diagram.

In order to register a new observation to a semantic octree, we follow the standard ray-casting procedure over an octree (Hornung et al. 2013) to find the observed leaf nodes. Then, for each observed leaf node, if the observation demands an update, the leaf node will be recursively expanded to the smallest resolution and the multi-class log-odds of the downstream nodes will be updated using (8). For ray's end

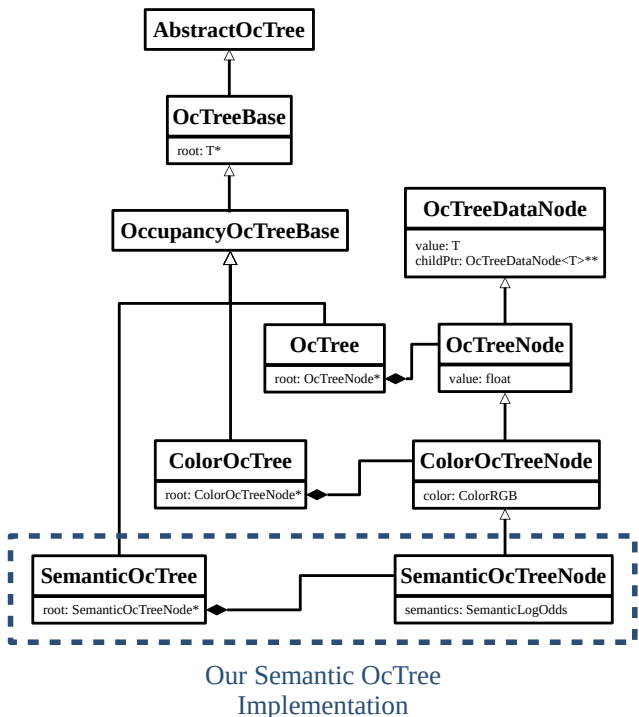


Figure 4. UML diagram showing the class inheritance used for the implementation of our semantic octree.

point, which indicates an occupied cell, we also update the *color* variable by averaging the observed color with the current stored color of the corresponding node. Alg. 2 details the probabilistic observation fusion procedure for our semantic octree.

It is necessary to define information propagation from children nodes towards parent (inner) nodes, so that a coarser representation of the OctoMap can be computed. This is useful for navigation where efficient collision checking is prioritized over detailed environment representation. Depending on the application, different information fusion strategies can be implemented. For example, a conservative strategy would assign multi-class log-odds of the child node with the most occupancy probability to the parent node. In this work, we simply assign the average log-odds vector of children nodes to their parent node as shown in Alg. 3.

* <https://octomap.github.io>

Algorithm 2 Semantic OcTree Update of Node \mathbf{n}_i

Input: $\mathbf{n}_i, \mathbf{z} = (r, y), \alpha$

- 1: $s = \mathbf{n}_i.semantics$
- 2: $s.d = \mathbf{n}_i.semantics.data$
- 3: $s.o = \mathbf{n}_i.semantics.others$
- 4: **if** \mathbf{z} indicates free **then**
- 5: Update s with ϕ^-
- 6: **else if** \mathbf{z} indicates class y **then**
- 7: Check if class y is among the 3 most likely classes in s and store the result in $isLikely$
- 8: **if** $isLikely$ **then**
- 9: Update s with $\phi^+ + \mathbf{E}_{y+1}\psi^+$
- 10: **else**
- 11: ▷ Derive h_{aux} as a portion α of $others$ class
- 12: $h_{aux} = s.o + \log \alpha$
- 13: $s.o += \phi_{others}^+ + \log(1 - \alpha)$
- 14: $s_c = \text{CONCAT}(s.d, (y, h_{aux}))$
- 15: Update s_c with $\phi^+ + \mathbf{E}_{y+1}\psi^+$
- 16: Perform descending sort on s_c with respect to log-odds values
- 17: ▷ Pick 3 most likely classes
- 18: $s.d = s_c[0 : 2]$
- 19: ▷ Combine the least likely class with $others$ class
- 20: $s.o = \log(\exp(s_c[3]) + \exp(s.o))$
- 21: ▷ Apply thresholds for log-odds values
- 22: MAXMINTHRESH(s)
- 23: $\mathbf{n}_i.semantics = s$
- 24: **return** \mathbf{n}_i

As mentioned earlier, the main benefit of the OctoMap representation is the possibility of combining similar cells (leaf nodes) into a large cell (inner node). This is called *pruning* the octree. Every time after an observation is integrated to the map, starting from the smallest (deepest) inner node, we check for each inner node if 1) the node has 8 children, 2) its children don't have any children of their own, and 3) its children all have equal multi-class log-odds. If an inner node satisfies all of these three criteria, its children will be pruned and the inner node will be converted to a leaf node with the same multi-class log-odds of its children. For mapping using range sensors, this helps to compress the majority of free cells into a few large cells; while occupied cells usually do not undergo pruning since only the surface of objects will be observed by the sensor, and their inside remains as unexplored region.

Remark Due to the sensor noise, it is unlikely that cells belonging to the same class (e.g. free or occupied by the same obstacle) attain identical multi-class log-odds. As suggested by Hornung et al. (2013), we apply maximum and minimum thresholds for the elements of the multi-class log-odds. As a result, each cell arrives at a stable state as its multi-class log-odds entries reach the maximum or minimum thresholds after a few number of observations; assuming that the environment is static, or the frequency of observations is greatly larger than the rate that the environment changes. The stable cells are more likely to share the same multi-class probability distribution since the thresholding limits the entries of their respective log-odds vectors; consequently increasing the chance of octree pruning. However, the

Algorithm 3 Semantic Fusion of Two Child Nodes

Input: $\mathbf{n}_i, \mathbf{n}_j$

- 1: $s_i = \mathbf{n}_i.semantics$
- 2: $s_j = \mathbf{n}_j.semantics$
- 3: $\mathcal{K}_f = \text{UNIQUECLASS}(s_i, s_j)$
- 4: $s_f = \text{SemanticLogOdds}()$
- 5: $o_i = s_i.o - \log(1 + \mathcal{K}_f.size - s_i.d.size)$
- 6: $o_j = s_j.o - \log(1 + \mathcal{K}_f.size - s_j.d.size)$
- 7: **for** $y \in \mathcal{K}_f$ **do**
- 8: **if** $y \notin s_i.d.label \wedge y \in s_j.d.label$ **then**
- 9: $s_f.d.APPEND(y, \frac{o_i + s_j.d[y].logOdds}{2})$
- 10: **else if** $y \in s_i.d.label \wedge y \notin s_j.d.label$ **then**
- 11: $s_f.d.APPEND(y, \frac{s_i.d[y].logOdds + o_j}{2})$
- 12: **else**
- 13: $s_f.d.APPEND(y, \frac{s_i.d[y].logOdds + s_j.d[y].logOdds}{2})$
- 14: $expOthers = \exp(\frac{o_i + o_j}{2})$
- 15: Perform descending sort on $s_f.d$ with respect to log-odds values
- 16: **for** $i > 3$ **do**
- 17: $expOthers += \exp(s_f.d[i].logOdds)$
- 18: $s_f.d[3 : end].REMOVE()$
- 19: $s_f.o = \log(expOthers)$
- 20: MAXMINTHRESH(s_f)
- 21: **return** s_f

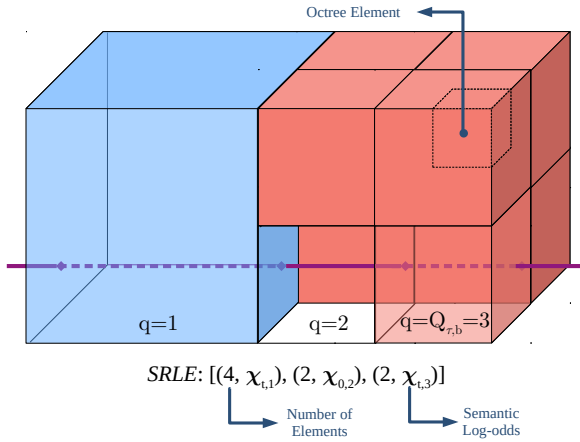


Figure 5. Ray cast representation as semantic run-length encoding (SRLE). The multi-class log-odds $\chi_{t,q}$ are uniform within each cube.

thresholds will cause a loss of information near $p_t(m_i = k) = 1, k \in \mathcal{K}$ which can be controlled by choosing the maximum and minimum thresholds.

6.2 Information Computation

A ray cast through an octree representation may visit several large cells within which the class probabilities are homogeneous. We exploit this property of an OctoMap in order to simplify the semantic information computation by obtaining the mutual information between the OctoMap and

a single ray as a summation over a subset of octree leaf nodes, instead of individual map cells. As we will show in this section, this simplification provides a significant gain in terms of performance with minimal loss of accuracy. The following formulation can be considered as a multi-class generalization of the run-length encoding (RLE) technique introduced by Zhang et al. (2019), using the semantic mutual information of (13) and the semantic OctoMap defined earlier in this section.

Assume that the map cells along a single beam $\mathbf{R}_\tau \eta_b$ have piece-wise constant class probabilities such that the set $\{m_i \mid i \in \mathcal{R}_{\tau,b}(r_{max})\}$ can be partitioned into $Q_{\tau,b}$ groups of consecutive cells indexed by $\mathcal{R}_{\tau,b}^q(r_{max})$ ($q = 1, \dots, Q_{\tau,b}$) where:

$$p_t(m_i = k) = p_t(m_j = k), \quad \forall i, j \in \mathcal{R}_{\tau,b}^q(r_{max}), \quad \forall k \in \mathcal{K}. \quad (14)$$

In this case, a ray cast can be sufficiently represented by a semantic run-length encoding, defined as below.

Definition 3. A *semantic run-length encoding* (SRLE) of ray $\mathbf{R}_\tau \eta_b$ is an ordered list of tuples of the form $[(\omega_{\tau,b,q}, \chi_{t,q})]_{q=1}^{Q_{\tau,b}}$, where $\omega_{\tau,b,q}$ and $\chi_{t,q}$ respectively represent the width and the log-odds vector of the intersection between the ray and the q -th partition. Furthermore, the width $\omega_{\tau,b,q}$ is defined as the number of octree *elements* along the intersection, where an octree element is a cell with the smallest physical dimensions.

Note that SRLE can be used in a general grid map representation. However, semantic OctoMap representation inherently contains large regions with homogeneous multi-class log-odds, which is the result of octree pruning. Additionally, the octree data structure allows for faster ray casting since it can be done over octree leaf nodes (Samet 1989; Agate et al. 1991), instead of casting a ray through a uniform resolution grid of cells as in Bresenham (1965). Therefore, semantic OctoMap would be a practical candidate for using SRLE ray casting. Fig 5 shows an example of ray cast representation as SRLE over a semantic OctoMap.

Utilizing SRLE ray casting delivers substantial gains in efficiency for semantic mutual information computation since the contribution of each group $\{m_i \mid i \in \mathcal{R}_{\tau,b}^q(r_{max})\}$ in the innermost summation of (13) can be obtained in closed form. The following proposition expresses mutual information computation over a semantic OctoMap.

Proposition 3. Let $\mathbf{z}_{\tau,b}$ be a single range-category measurement. Then, the Shannon mutual information between $\mathbf{z}_{\tau,b}$ and a semantic OctoMap \mathbf{m} can be computed as:

$$I(\mathbf{m}; \mathbf{z}_{\tau,b} \mid \mathcal{Z}_{1:t}) = \sum_{k=1}^K \sum_{q=1}^{Q_{\tau,b}} \rho_{\tau,b}(q, k) \Theta_{\tau,b}(q, k) \quad (15)$$

where $Q_{\tau,b}$ is the number of partitions along the ray $\mathbf{R}_\tau \eta_b$ that have identical multi-class log-odds and the multi-class probabilities for each partition are denoted as:

$$\begin{cases} \pi_t(q, k) = p_t(m_i = k) & \forall i \in \mathcal{R}_{\tau,b}^q(r_{max}) \\ \chi_{t,q} = \mathbf{h}_{t,i} \end{cases}$$

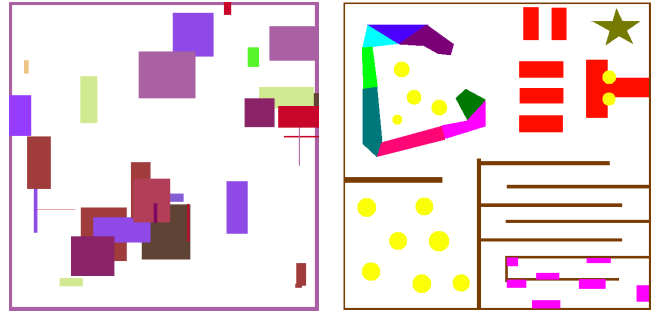


Figure 6. Synthetic environments used for comparisons among frontier-based exploration (Yamauchi 1997), FSMI (Zhang et al. 2019), and our approach. Different semantic categories are represented by distinct colors. Left: An instance of procedurally generated random environment. Right: Hand designed environment with specific structures such as corridors and blocks.

Furthermore, defining $\omega_{\tau,b,q} = |\mathcal{R}_{\tau,b}^q(r_{max})|$ as the width of q -th partition, we have:

$$\begin{aligned} \rho_{\tau,b}(q, k) &:= \pi_t(q, k) \prod_{j=1}^{q-1} \pi_t^{\omega_{\tau,b,j}}(j, 0), \\ \Theta_{\tau,b}(q, k) &:= \beta_{\tau,b}(q, k) \frac{1 - \pi_t^{\omega_{\tau,b,q}}(q, 0)}{1 - \pi_t(q, 0)} + \\ &\quad \frac{f(\phi^- - \chi_{0,q}, \chi_{t,q})}{(1 - \pi_t(q, 0))^2} \left[(\omega_{\tau,b,q} - 1) \pi_t^{\omega_{\tau,b,q}+1}(q, 0) \right. \\ &\quad \left. - \omega_{\tau,b,q} \pi_t^{\omega_{\tau,b,q}}(q, 0) + \pi_t(q, 0) \right], \\ \beta_{\tau,b}(q, k) &:= f(\phi^+ + \mathbf{E}_{k+1} \psi^+ - \chi_{0,q}, \chi_{t,q}) \\ &\quad + \sum_{j=1}^{q-1} \omega_{\tau,b,j} f(\phi^- - \chi_{0,j}, \chi_{t,j}). \end{aligned}$$

Proof. See Appendix C.

The below corollary is a natural extension of (13) to semantic OctoMap representations. The proof follows directly from the additive property of mutual information between a semantic OctoMap and a sequence of independent observations.

Corollary 1. Given a sequence of labeled range observations $\mathcal{Z}_{t+1:t+T}$, the Shannon mutual information between $\mathcal{Z}_{t+1:t+T}$ and a semantic OctoMap \mathbf{m} can be lower bounded as:

$$\begin{aligned} I(\mathbf{m}; \mathcal{Z}_{t+1:t+T} \mid \mathcal{Z}_{1:t}) &\geq I(\mathbf{m}; \underline{\mathcal{Z}}_{t+1:t+T} \mid \mathcal{Z}_{1:t}) \\ &= \sum_{\tau=t+1}^{t+T} \sum_{b=1}^B \sum_{k=1}^K \sum_{q=1}^{Q_{\tau,b}} \rho_{\tau,b}(q, k) \Theta_{\tau,b}(q, k), \end{aligned} \quad (16)$$

where $\underline{\mathcal{Z}}_{t+1:t+T}$ is a subset of non-overlapping measurements that satisfy (12).

The same approach as in Alg. 1 is used for autonomous semantic exploration over an OctoMap. However, we employ the information computation formula of (16) in order to calculate the information gain of any candidate robot trajectory.

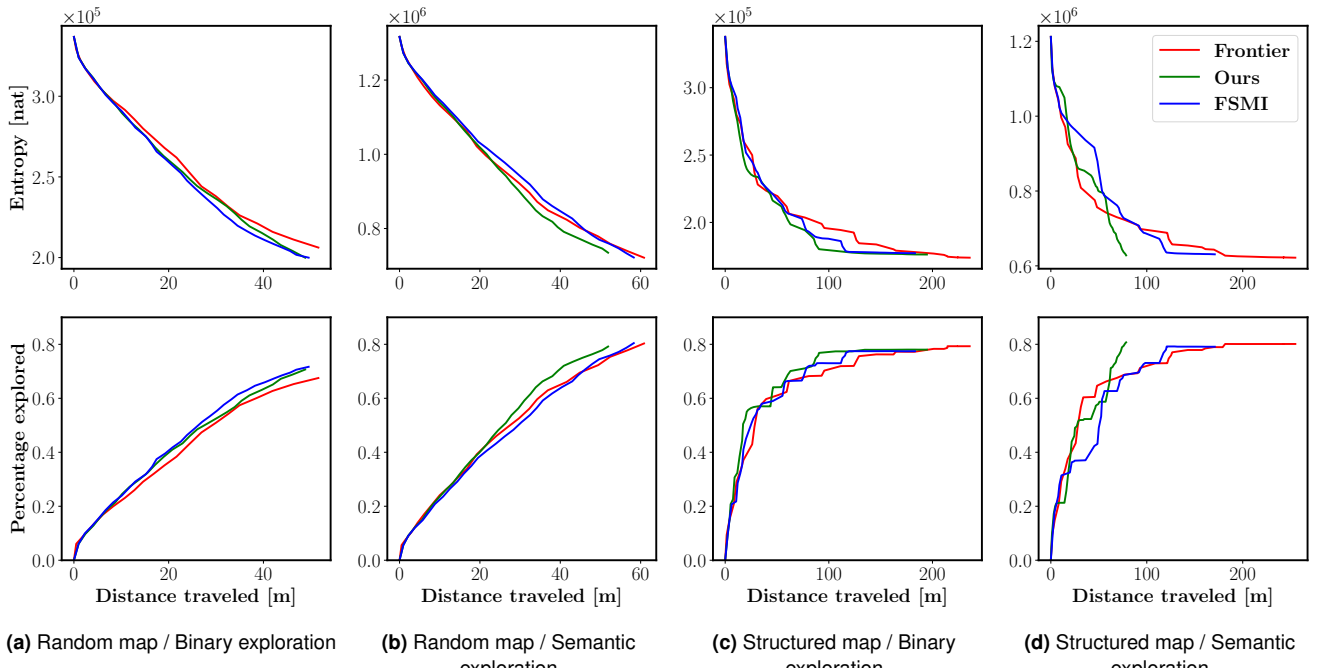


Figure 7. Simulation results for active mapping on the environments in Fig. 6. (a), (b): Exploration performance averaged over 10 random environments with 3 random starting positions for each instance. (c), (d): Exploration performance on the structured environment averaged over 3 random starting positions.

6.3 Computational Complexity

We first establish that mutual information in both (13) and (16) can be calculated recursively. For (13), we have:

$$\begin{aligned}
 p_{\tau,b}(n+1, k) &= p_{\tau,b}(n, k) \\
 &\times \frac{p_t(m_{j_{\tau,b}^*} = k)p_t(m_{i_{\tau,b}^*} = 0)}{p_t(m_{i_{\tau,b}^*} = k)}, \\
 C_{\tau,b}(n+1, k) &= C_{\tau,b}(n, k) \\
 &- f(\phi^+ + \mathbf{E}_{k+1}\psi^+ - \mathbf{h}_{0,i_{\tau,b}^*}, \mathbf{h}_{t,i_{\tau,b}^*}) \\
 &+ f(\phi^+ + \mathbf{E}_{k+1}\psi^+ - \mathbf{h}_{0,j_{\tau,b}^*}, \mathbf{h}_{t,j_{\tau,b}^*}) \\
 &+ f(\phi^- - \mathbf{h}_{0,i_{\tau,b}^*}, \mathbf{h}_{t,i_{\tau,b}^*}),
 \end{aligned} \tag{17}$$

where $j_{\tau,b}^*$ and $i_{\tau,b}^*$ correspond to the index of farthest map cell in $\tilde{\mathcal{R}}_{\tau,b}(n+1)$ and $\tilde{\mathcal{R}}_{\tau,b}(n)$, respectively. A similar recursive pattern can be found in (16):

$$\begin{aligned}
 \rho_{\tau,b}(q+1, k) &= \rho_{\tau,b}(q, k) \\
 &\times \frac{\pi_t(q+1, k)\pi_t^{\omega_{\tau,b,q}}(q, 0)}{\pi_t(q, k)}, \\
 \beta_{\tau,b}(q+1, k) &= \beta_{\tau,b}(q, k) \\
 &- f(\phi^+ + \mathbf{E}_{k+1}\psi^+ - \chi_{0,q}, \chi_{t,q}) \\
 &+ f(\phi^+ + \mathbf{E}_{k+1}\psi^+ - \chi_{0,q+1}, \chi_{t,q+1}) \\
 &+ \omega_{\tau,b,q}f(\phi^- - \chi_{0,q}, \chi_{t,q}).
 \end{aligned} \tag{18}$$

This implies that the innermost summations of (13) and (16) can be obtained in $O(N_{\tau,b})$ and $O(Q_{\tau,b})$, respectively. In an environment containing K object classes, a planning step composed of T observations, where each observation contains B beams, has a complexity of $O(TBKN_{\tau,b})$ for regular grid multi-class representation and a complexity of $O(TBKQ_{\tau,b})$ for semantic OctoMap representation.

As we will demonstrate in Sec. 7, for a ray $\mathbf{R}_{\tau}\eta_b$ we often observe that $Q_{\tau,b}$ is significantly smaller than $N_{\tau,b}$ thanks to the pruning mechanism. Also, note that $N_{\tau,b}$ scales linearly with the map resolution. Therefore, the complexity of information computation over a semantic OctoMap grows sub-linearly with regards to the size of octree elements, which is a parameter analogous to the map resolution.

7 Experiments

In this section we evaluate performance of the proposed semantic exploration method in a variety of simulated and real-world experiments. We also examine two baseline exploration strategies: frontier-based exploration (Frontier) (Yamauchi 1997) and FSMI (Zhang et al. 2019) as comparison to our method. We compare the methods in a 2-D active binary mapping scenario in Sec. 7.1 and 2-D active multi-class mapping scenario in Sec. 7.2. All three methods use our range-category sensor model in (10) and our Bayesian multi-class mapping in (8) but select informative robot trajectories $\mathbf{X}_{t+1:t+T}(\mathbf{u}_{t:t+T-1})$ based on their own criteria. In Sec. 7.3, we evaluate the improvement in ray-tracing resulting from using SRLE through an experiment in a 3-D simulated Unity environment. Additionally, in Sec. 7.4, we apply our method in a similar 3-D simulation environment to demonstrate large-scale realistic active multi-class mapping using the proposed octree-based semantic information computation of Sec. 6. Finally, in Sec. 7.5, we test our semantic exploration method in a real world environment using a robot rover.

In each planning step of 2-D exploration, we identify frontiers by applying edge detection on the most likely map at time t (the mode of $p_t(\mathbf{m})$). Then, we cluster the edge cells by detecting the connected components of the boundaries between explored and unexplored space. We plan a path from the robot pose \mathbf{X}_t to the center of each frontier using

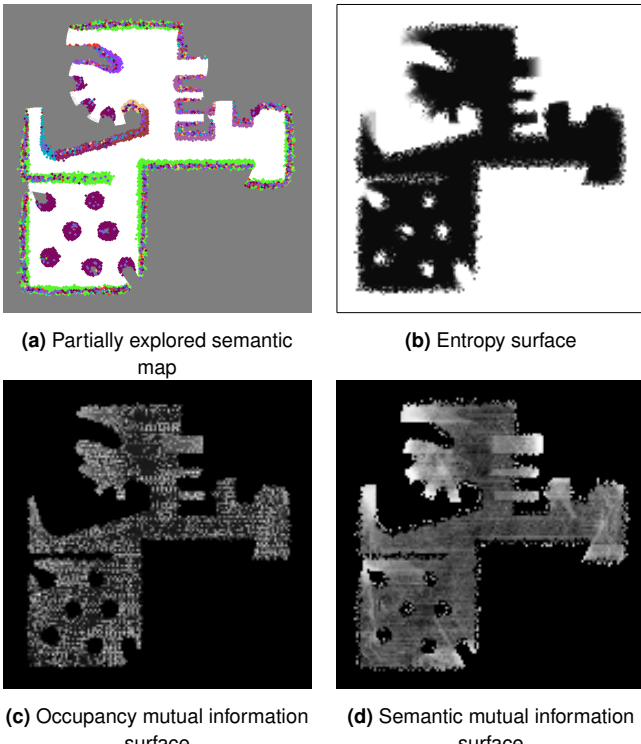


Figure 8. A snapshot of 2-D exploration. In sub-figure (b), the entropy for each pixel i is computed as (19). Sub-figure (c) and (d) show the mutual information used to find the informative trajectory by FSMI and our method, respectively. Brighter pixels indicate larger values.

A^* graph search and provide it to a low-level controller to generate $\mathbf{u}_{t:t+T-1}$. For 3-D exploration, we first derive a 2-D occupancy map by projecting the most likely semantic OctoMap at time t onto $z = 0$ surface and proceed with similar steps as in 2-D path planning.

7.1 2-D Binary Exploration

We consider active binary occupancy mapping first. We compare our method against Frontier and FSMI in 1 structured and 10 procedurally generated 2-D environments (Fig. 6). A 2-D LiDAR sensor is simulated with additive Gaussian noise $\mathcal{N}(0, 0.1)$. Fig. 7 (a) and Fig. 7 (c) compare exploration performance in terms of the map entropy reduction and percentage of the map explored per distance traveled among the three methods. Our method performs similarly to FSMI in that both achieve low map entropy by traversing significantly less distance compared to Frontier.

7.2 2-D Multi-class Exploration

Next, we use the same 2-D environments in Fig. 6 but introduce range-category measurements. Range measurements are subject to additive Gaussian noise $\mathcal{N}(0, 0.1)$, while category measurement have a uniform misclassification probability of 0.35. Fig. 7 (b) and Fig. 7 (d) compare the semantic exploration performance for all three strategies. Our method reaches the same level of map entropy as FSMI and Frontier but traverses a noticeable shorter distance. This can be attributed to the fact that only our method distinguishes map cells whose occupancy probabilities are the same but their per-class probabilities differ from each other. To further illustrate this, we visualize the entropy and

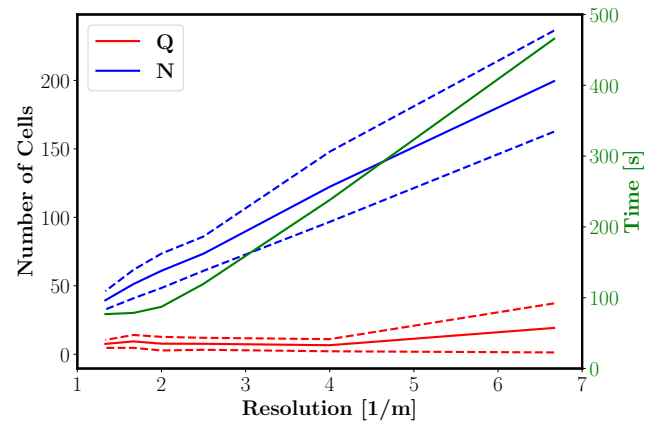


Figure 9. Variations of visited OctoMap cells and octree elements denoted as Q and N , respectively, with respect to the map resolution. Solid blue and red lines represent the average values for Q and N over all ray-castings, while the dashed lines show 1 standard deviation from the average. The green curve shows total exploration time for each map resolution. All measurements are accumulated in the course of 5 exploration iterations.

information surfaces used by FSMI and our method. Fig. 8 (a) shows a snapshot of semantic exploration while Fig. 8 (b) visualizes the entropy of each pixel i computed as:

$$H(m_i) = - \sum_{k=0}^K p(m_i = k) \log p(m_i = k) \quad (19)$$

The task of exploration can be regarded as minimizing the cumulative entropy of all pixels, i.e. map entropy. The reduction in map entropy can be estimated by the mutual information between the map and (unrealized) observations. Therefore, the exploration performance is highly dependent upon the mutual information formulation. As shown in Fig. 8 (d), our semantic mutual information, computed in (13) provides a smoother and more accurate estimation of information-rich regions compared to the mutual information formula used by FSMI (equation (18) in Zhang et al. (2019)) shown in Fig. 8 (c).

7.3 SRLE Compression for 3-D Ray-tracing

In this subsection, we evaluate the ray-tracing compression resulting from SRLE through an experiment in a photo-realistic 3-D Unity simulation, shown in Fig. 10 (e). We use a Husky robot equipped with an RGBD camera and run a semantic segmentation algorithm over the RGB images. In order to remove irrelevant randomness, the sensors and the semantic segmentation are defined as error-free. We define *map resolution* as the inverse of the dimensions of an octree element. For resolutions ranging from $1.3m^{-1}$ to $6.6m^{-1}$, we run 5 exploration iterations using the semantic OctoMap and information computation of Sec. 6 and store all ray-tracings in SRLE format. Fig. 5 shows the change in distribution for the number of OctoMap cells Q and octree elements N visited during each ray-tracing, as well as the time required to execute each exploration episode as a function of map resolution. In other words, N represents the number of cells to be processed during mapping and information computation as if the environment was represented as a regular 3-D grid, while Q represents the actual number of

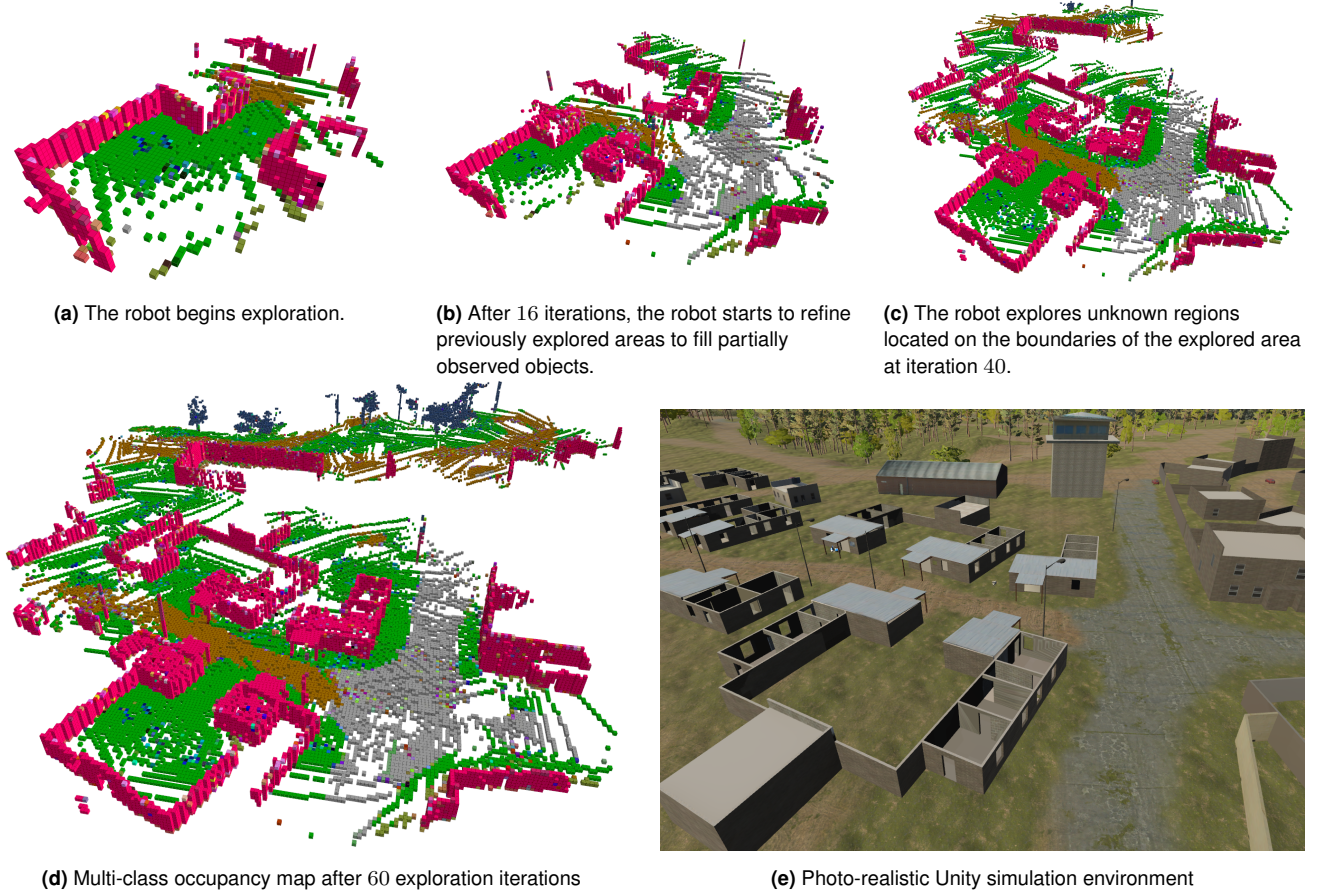


Figure 10. Time lapse of autonomous exploration and multi-class mapping in a simulated Unity environment. The robot is equipped with an RGBD sensor and runs semantic segmentation. Different colors represent different semantic categories (grass, dirt road, building, etc.).

processed semantic OctoMap cells. As expected, the pruning mechanism of the octree-based representation results in a substantial gain in terms of the number of cells visited for each ray-tracing. Moreover, as opposed to the almost linear growth of N , the distribution for Q is effectively independent of the map resolution, except for very fine resolutions where void areas between observations rays prevent efficient pruning. However, for map resolutions larger than $2m^{-1}$, the exploration time tends to grow larger with the increase of map resolution. This is attributed to the recursive ray insertion method of OctoMap in which it is required to re-compute log odds for each octree element along an observation ray whenever an observation ray does not carry the same (free or object class) state as the visited cell. In the subsequent 3-D experiments, we choose map resolution of $2m^{-1}$ in order to balance between performance and map accuracy.

7.4 3-D Exploration in Unity Simulation

Here we evaluate our active multi-class mapping algorithm in the same 3-D simulation environment as the previous subsection; however, this time the range measurements have an additive Gaussian noise of $\mathcal{N}(0, 0.1)$ and the semantic segmentation algorithm detects the true class with a probability of 0.95. Fig. 10 (a)-(d) shows several iterations of the exploration process. Fig. 11 shows the change in map entropy versus distance traveled and elapsed time for our method and frontier-based exploration. We observe that our

method is more efficient in terms of solving the trade-off between path length and the information gathered along the path. On the other hand, our method requires evaluation of mutual information along each candidate trajectory, while frontier-based simply chooses the trajectory leading to the largest frontier. As a result, frontier-based exploration can be performed over a shorter time period compared to ours. Fig. 12 compares the classification precision between our method and frontier-based. In general, our method exhibits higher precision for object categories that appear sparsely, such as *Animal* or *Tree* classes while frontier-based slightly outperforms our method when it comes to mapping the ground surface. This can be ascribed to the algorithmic tendency of our method towards achieving high overall classification precision even if it requires slight reduction of precision for certain object categories.

7.5 3-D Exploration in Real-world

We deployed our proposed semantic exploration method in a real-world platform. Fig. 13 shows the robotic platform used for running the experiments powered by the NVIDIA Xavier NX edge computing module. A mounted Hokuyo UST-10LX LiDAR is used for localization via ICP laser scan matching (Censi 2008). The robot car is also equipped with an Intel RealSense D435i RGBD camera which provides 2-D color image and depth map. We deployed a semantic segmentation neural network based on a *ResNet18* architecture (He et al. 2016) and trained on the SUN RGB-D dataset (Song et al.

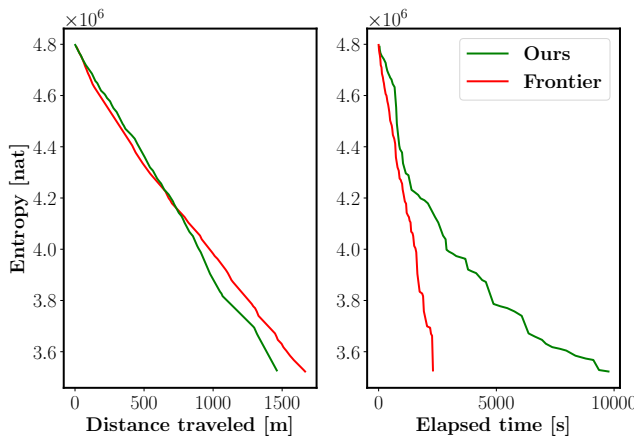


Figure 11. Simulation results for active mapping in Unity 3-D environment.

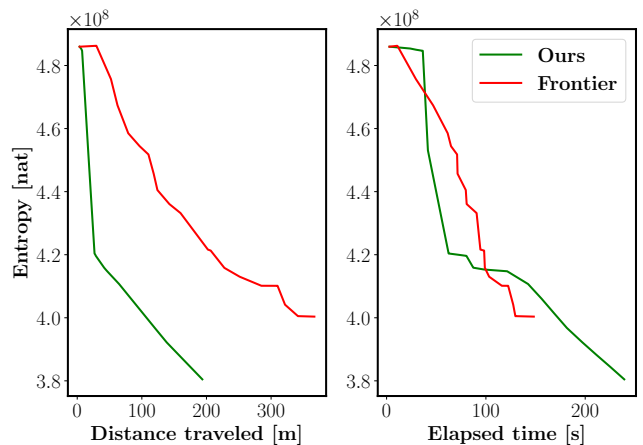


Figure 14. Real-world experiment results for active mapping for 20 exploration iterations.

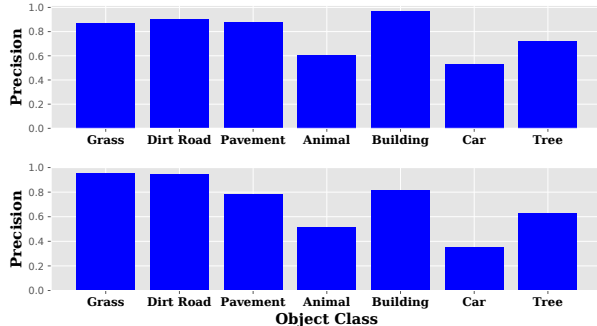


Figure 12. Precision for observed semantic classes. (top): Our method (bottom): Frontier



Figure 13. 1/10 scale robot car used for real-world experiments.

2015). The semantic segmentation algorithm takes a 2-D color image and outputs a semantic label for each pixel in the image. By aligning the semantic image and the depth map, we derive a semantic 3-D point cloud which is utilized by our Bayesian multi-class mapping method. Fig. 15 depicts the exploration process, while Fig. 14 shows the performance of our method compared to frontier-based over 20 exploration iterations. We observe that, similar to the simulations, our method outperforms frontier-based exploration in terms of distance traveled. Unlike the simulated experiments, our method has shown relatively on par performance compared to frontier-based with regards to entropy reduction over

time. This can be explained by the fact that large depth measurement noise and classification error in the real-world experiments result in (a) the need for re-visiting explored areas in order to estimate an accurate map, leading to poor entropy reduction for frontier-based method and (b) a small number of safe candidate trajectories, leading to less computations to be processed by our method.

8 Conclusion

This paper developed techniques for active multi-class mapping of large 3-D environments using range and semantic segmentation observations. Our results enable efficient mutual information computation over multi-class maps and make it possible to optimize for per-class uncertainty. Our experiments show that the proposed method performs on par with the state of the art FSMI method in binary active mapping scenarios. However, when semantic information is considered our method outperforms existing algorithms and leads to efficient exploration and accurate multi-class mapping. Moreover, experiments in both simulated and real-world environments proved the scalability of the proposed OcTree-based mapping and information computation methods for large-scale 3-D exploration scenarios.

References

- Agate M, Grimsdale RL and Lister PF (1991) The hero algorithm for ray-tracing octrees. In: *Advances in Computer Graphics Hardware IV*. pp. 61–73.
- Atanasov N, Le Ny J, Daniilidis K and Pappas GJ (2015) Decentralized active information acquisition: Theory and application to multi-robot SLAM. In: *IEEE International Conference on Robotics and Automation (ICRA)*. pp. 4775–4782.
- Blum H, Rohrbach S, Popovic M, Bartolomei L and Siegwart RY (2019) Active learning for uav-based semantic mapping. *ArXiv* abs/1908.11157.
- Bourgault F, Makarenko AA, Williams SB, Grocholsky B and Durrant-Whyte HF (2002) Information based adaptive robotic exploration. In: *IEEE/RSJ International Conference on Intelligent Robots and Systems (IROS)*. pp. 540–545.

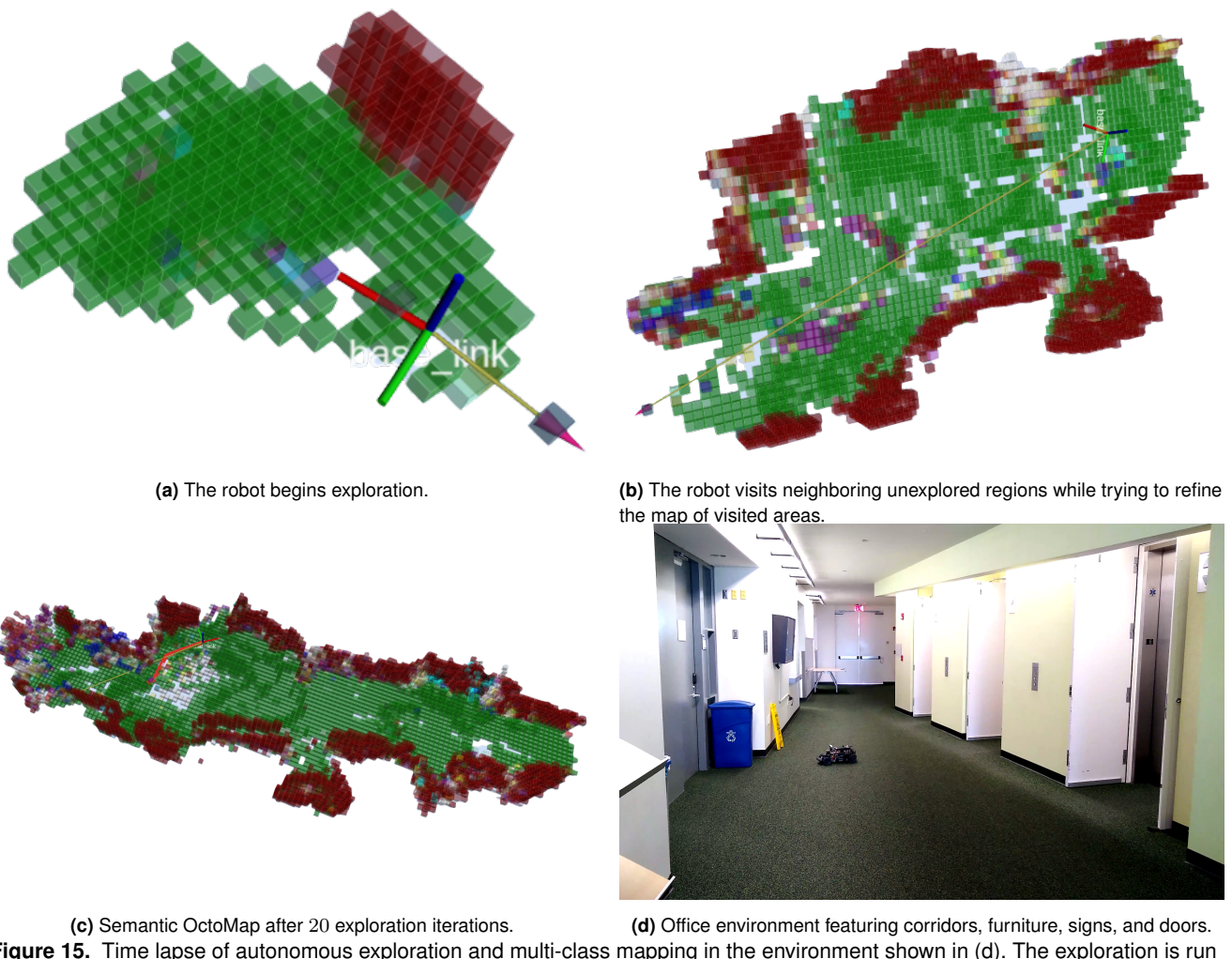


Figure 15. Time lapse of autonomous exploration and multi-class mapping in the environment shown in (d). The exploration is run for 20 iterations. Different colors represent different semantic categories (floor, wall, furniture, etc.).

Bresenham JE (1965) Algorithm for computer control of a digital plotter. *IBM Systems Journal* 4(1): 25–30.

Burgard W, Moors M, Stachniss C and Schneider FE (2005) Coordinated multi-robot exploration. *IEEE Transactions on Robotics (TRO)* 21(3): 376–386.

Cao C, Zhang J, Travers M and Choset H (2020) Hierarchical coverage path planning in complex 3d environments. In: *IEEE International Conference on Robotics and Automation (ICRA)*.

Carbone L, Du J, Ng MK, Bona B and Indri M (2014) Active SLAM and exploration with particle filters using Kullback–Leibler divergence. *Journal of Intelligent & Robotic Systems* 75(2): 291–311.

Carrillo H, Reid I and Castellanos JA (2012) On the comparison of uncertainty criteria for active slam. In: *IEEE International Conference on Robotics and Automation (ICRA)*. pp. 2080–2087.

Censi A (2008) An icp variant using a point-to-line metric. In: *IEEE International Conference on Robotics and Automation (ICRA)*. pp. 19–25.

Charrow B, Liu S, Kumar V and Michael N (2015) Information-theoretic mapping using cauchy-schwarz quadratic mutual information. In: *IEEE International Conference on Robotics and Automation (ICRA)*. pp. 4791–4798.

Elfes A (1989) Using occupancy grids for mobile robot perception and navigation. *Computer* 22(6): 46–57.

Elfes A (1995) Robot navigation: Integrating perception, environmental constraints and task execution within a probabilistic framework. In: *Reasoning With Uncertainty in Robotics*. pp. 93–130.

Gan L, Zhang R, Grizzle JW, Eustice RM and Ghaffari M (2020) Bayesian spatial kernel smoothing for scalable dense semantic mapping. *IEEE Robotics and Automation Letters* 5(2): 790–797.

Georgakis G, Bucher B, Schmeckpeper K, Singh S and Daniilidis K (2021) Learning to map for active semantic goal navigation. *ArXiv* abs/2106.15648.

Gómez C, Fehr M, Hernández AC, Nieto J, Barber R and Siegwart R (2020) Hybrid Topological and 3D Dense Mapping through Autonomous Exploration for Large Indoor Environments. In: *IEEE International Conference on Robotics and Automation (ICRA)*.

González-Baños HH and Latombe JC (2002) Navigation strategies for exploring indoor environments. *The International Journal of Robotics Research (IJRR)* 21(10-11): 829–848. DOI:10.1177/0278364902021010834.

He K, Zhang X, Ren S and Sun J (2016) Deep residual learning for image recognition. In: *Proceedings of the IEEE conference on computer vision and pattern recognition*. pp. 770–778.

Henderson T, Sze V and Karaman S (2020) An efficient and continuous approach to information-theoretic exploration. In: *IEEE International Conference on Robotics and Automation (ICRA)*.

(ICRA).

Hornung A, Wurm KM, Bennewitz M, Stachniss C and Burgard W (2013) OctoMap: an efficient probabilistic 3D mapping framework based on octrees. *Autonomous Robots* 34: 189–206.

Julian BJ, Karaman S and Rus D (2013) On mutual information-based control of range sensing robots for mapping applications. In: *IEEE/RSJ International Conference on Intelligent Robots and Systems (IROS)*. pp. 5156–5163.

Kollar T and Roy N (2008) Efficient optimization of information-theoretic exploration in slam. In: *AAAI Conference on Artificial Intelligence*. p. 1369–1375.

Maffei R, Souza MP, Mantelli M, Pittol D, Kolberg M and Jorge VAM (2020) Exploration of 3D terrains using potential fields with elevation-based local distortions. In: *IEEE International Conference on Robotics and Automation (ICRA)*.

Milioto A and Stachniss C (2019) Bonnet: An Open-Source Training and Deployment Framework for Semantic Segmentation in Robotics using CNNs. In: *IEEE International Conference on Robotics and Automation (ICRA)*.

Moorehead SJ, Simmons R and Whittaker WL (2001) Autonomous exploration using multiple sources of information. In: *IEEE International Conference on Robotics and Automation (ICRA)*. pp. 3098–3103.

Samet H (1989) Implementing ray tracing with octrees and neighbor finding. *Computers & Graphics* 13(4): 445–460.

Song S, Lichtenberg SP and Xiao J (2015) Sun rgb-d: A rgb-d scene understanding benchmark suite. In: *Proceedings of the IEEE conference on computer vision and pattern recognition*. pp. 567–576.

Song S, Yu F, Zeng A, Chang AX, Savva M and Funkhouser T (2017) Semantic scene completion from a single depth image. In: *IEEE Conference on Computer Vision and Pattern Recognition (CVPR)*. pp. 1746–1754.

Stachniss C, Grisetti G and Burgard W (2005) Information gain-based exploration using Rao-Blackwellized particle filters. In: *Robotics: Science and Systems*. pp. 65–72.

Suriani V, Kaszuba S, Sabbella SR, Riccio F and Nardi D (2021) S-ave: Semantic active vision exploration and mapping of indoor environments for mobile robots. In: *2021 European Conference on Mobile Robots (ECMR)*. pp. 1–8.

Thrun S (2003) Learning occupancy grid maps with forward sensor models. *Autonomous Robots* 15(2): 111–127.

Thrun S, Burgard W and Fox D (2005) *Probabilistic Robotics*. MIT Press Cambridge.

Veiga TS, Silva M, Ventura R and Lima PU (2021) A hierarchical approach to active semantic mapping using probabilistic logic and information reward pomdps. *Proceedings of the International Conference on Automated Planning and Scheduling* 29(1): 773–781.

Visser A and Slamet B (2008) Balancing the information gain against the movement cost for multi-robot frontier exploration. In: *European Robotics Symposium*. pp. 43–52. DOI:10.1007/978-3-540-78317-6_5.

Wang J, Shan T and Englot B (2019) Virtual maps for autonomous exploration with pose slam. In: *IEEE/RSJ International Conference on Intelligent Robots and Systems*.

Wang T, Dhiman V and Atanasov N (2020) Learning navigation costs from demonstration with semantic observations. *Proceedings of Machine Learning Research* vol 120: 1–11.

Yamauchi B (1997) A frontier-based approach for autonomous exploration. In: *IEEE International Symposium on Computational Intelligence in Robotics and Automation*. pp. 146–151.

Zhang Z, Henderson T, Sze V and Karaman S (2019) Fsmi: Fast computation of shannon mutual information for information-theoretic mapping. In: *IEEE International Conference on Robotics and Automation (ICRA)*. pp. 6912–6918.

Appendix A Proof of Prop. 1

Applying Bayes rule in (2) and the factorization in (5) to $p_t(\mathbf{m})$ for some $\mathbf{z} \in \mathcal{Z}_{t+1}$ leads to:

$$\prod_{i=1}^N p(m_i | \mathcal{Z}_{1:t}, \mathbf{z}) = \frac{p(\mathbf{z})}{p(\mathbf{z} | \mathcal{Z}_{1:t})} \prod_{i=1}^N \frac{p(m_i | \mathbf{z})}{p(m_i)} p(m_i | \mathcal{Z}_{1:t}). \quad (20)$$

The term $\frac{p(\mathbf{z})}{p(\mathbf{z} | \mathcal{Z}_{1:t})}$ may be eliminated by considering the odds ratio of the cell probabilities:

$$\begin{aligned} & \prod_{i=1}^N \frac{p(m_i = k_i | \mathcal{Z}_{1:t}, \mathbf{z})}{p(m_i = 0 | \mathcal{Z}_{1:t}, \mathbf{z})} \\ &= \prod_{i=1}^N \frac{p(m_i = k_i | \mathbf{z})}{p(m_i = 0 | \mathbf{z})} \frac{p(m_i = 0)}{p(m_i = k_i)} \frac{p(m_i = k_i | \mathcal{Z}_{1:t})}{p(m_i = 0 | \mathcal{Z}_{1:t})}. \end{aligned} \quad (21)$$

Since each term in both the left- and right-hand side products only depends on one map cell m_i , the expression holds for each individual cell. Re-writing the expression for cell m_i in vector form, with elements corresponding to each possible value of $k_i \in \mathcal{K}$, and taking an element-wise log leads to:

$$\begin{aligned} & \left[\log \frac{p(m_i=0 | \mathcal{Z}_{1:t}, \mathbf{z})}{p(m_i=0 | \mathcal{Z}_{1:t}, \mathbf{z})} \quad \dots \quad \log \frac{p(m_i=K | \mathcal{Z}_{1:t}, \mathbf{z})}{p(m_i=0 | \mathcal{Z}_{1:t}, \mathbf{z})} \right]^\top \\ &= (\mathbf{l}_i(\mathbf{z}) - \mathbf{h}_{0,i}) + \mathbf{h}_{t,i} \end{aligned} \quad (22)$$

Applying (22) recursively for each element $\mathbf{z} \in \mathcal{Z}_{t+1}$ leads to the desired result in (8). \square

Appendix B Proof of Prop. 2

Let $\mathcal{R}_{t+1:t+T}(r_{max}) := \cup_{\tau,b} \mathcal{R}_{\tau,b}(r_{max})$ be the set of map indices which can potentially be observed by $\mathcal{Z}_{t+1:t+T}$. Using the factorization in (5) and the fact that Shannon entropy is additive for mutually independent random variables, the mutual information only depends on the cells whose index belongs to $\mathcal{R}_{t+1:t+T}(r_{max})$, i.e.:

$$\begin{aligned} & I(\mathbf{m}; \mathcal{Z}_{t+1:t+T} | \mathcal{Z}_{1:t}) \\ &= \sum_{\tau=t+1}^{t+T} \sum_{b=1}^B \sum_{i \in \mathcal{R}_{\tau,b}(r_{max})} I(m_i; \mathbf{z}_{\tau,b} | \mathcal{Z}_{1:t}). \end{aligned} \quad (23)$$

This is true because the measurements $\mathbf{z}_{\tau,b} \in \mathcal{Z}_{t+1:t+T}$ are independent by construction and the terms $I(m_i; \mathcal{Z}_{t+1:t+T} | \mathcal{Z}_{1:t})$ can be decomposed into sums of mutual information terms between single-beam measurements $\mathbf{z}_{\tau,b}$ and the respective observed map cells m_i . The mutual information between a single map cell m_i and a sensor ray \mathbf{z} is equal to:

$$\begin{aligned} & I(m_i; \mathbf{z} | \mathcal{Z}_{1:t}) = \\ & \int p(\mathbf{z} | \mathcal{Z}_{1:t}) \sum_{k=0}^K p(m_i = k | \mathbf{z}, \mathcal{Z}_{1:t}) \log \frac{p(m_i = k | \mathbf{z}, \mathcal{Z}_{1:t})}{p_t(m_i = k)} d\mathbf{z}. \end{aligned} \quad (24)$$

Using the inverse observation model in (10) and the Bayesian multi-class update in (8), we have:

$$\begin{aligned} & \sum_{k=0}^K p(m_i = k \mid \mathbf{z}, \mathcal{Z}_{1:t}) \log \frac{p(m_i = k \mid \mathbf{z}, \mathcal{Z}_{1:t})}{p_t(m_i = k)} \\ &= (\mathbf{l}_i(\mathbf{z}) - \mathbf{h}_{0,i})^\top \sigma(\mathbf{l}_i(\mathbf{z}) - \mathbf{h}_{0,i} + \mathbf{h}_{t,i}) + \log \frac{p(m_i = 0 \mid \mathbf{z}, \mathcal{Z}_{1:t})}{p_t(m_i = 0)} \\ &= f(\mathbf{l}_i(\mathbf{z}) - \mathbf{h}_{0,i}, \mathbf{h}_{t,i}), \end{aligned} \quad (25)$$

where (10) and (8) were applied a second time to the log term above. Plugging (25) back into the mutual information expression in (24) and returning to (23), we have:

$$\begin{aligned} & I(\mathbf{m}; \mathcal{Z}_{t+1:t+T} \mid \mathcal{Z}_{1:t}) \quad (26) \\ &= \sum_{\tau=t+1}^{t+T} \sum_{b=1}^B \sum_{y=1}^K \int_0^{r_{max}} \left(p(\mathbf{z}_{\tau,b} = (r, y) \mid \mathcal{Z}_{1:t}) \right. \\ & \quad \left. \sum_{i \in \mathcal{R}_{\tau,b}(r_{max})} f(\mathbf{l}_i((r, y)) - \mathbf{h}_{0,i}, \mathbf{h}_{t,i}) \right) dr. \end{aligned}$$

For $\mathbf{z}_{\tau,b} = (r, y)$, the second term inside the integral above can be simplified to:

$$\begin{aligned} \tilde{C}_{\tau,b}(r, y) &:= \sum_{i \in \mathcal{R}_{\tau,b}(r_{max})} f(\mathbf{l}_i((r, y)) - \mathbf{h}_{0,i}, \mathbf{h}_{t,i}) \\ &= f(\phi^+ + \mathbf{E}_{y+1} \psi^+ - \mathbf{h}_{0,i_{\tau,b}}, \mathbf{h}_{t,i_{\tau,b}}) \quad (27) \\ & \quad + \sum_{i \in \mathcal{R}_{\tau,b}(r) \setminus \{i_{\tau,b}^*\}} f(\phi^- - \mathbf{h}_{0,i}, \mathbf{h}_{t,i}) \end{aligned}$$

because for map indices $i \in \mathcal{R}_{\tau,b}(r_{max}) \setminus \mathcal{R}_{\tau,b}(r)$ that are not observed by $\mathbf{z}_{\tau,b}$, we have $\mathbf{l}_i((r, y)) = \mathbf{h}_{0,i}$ according to (10) and $f(\mathbf{h}_{0,i} - \mathbf{h}_{0,i}, \mathbf{h}_{t,i}) = 0$.

Next, we apply the approximation of (11) for the first term in the integral in (26); which leads to integration over $\tilde{p}_{\tau,b}(r, y) \tilde{C}_{\tau,b}(r, y)$ in (26). Note that $\tilde{p}_{\tau,b}(r, y)$ and $\tilde{C}_{\tau,b}(r, y)$ are piece-wise constant functions since $\mathcal{R}_{\tau,b}(r)$ is constant with respect to r as long as the beam \mathbf{z} lands in cell m_{i^*} . Hence, we can partition the integration domain over r into a union of intervals where the beam \mathbf{z} hits the same cell, i.e. $\mathcal{R}_{\tau,b}(r)$ remains constant:

$$\int_0^{r_{max}} \tilde{p}_{\tau,b}(r, y) \tilde{C}_{\tau,b}(r, y) dr = \sum_{n=1}^{N_{\tau,b}} \int_{r_{n-1}}^{r_n} \tilde{p}_{\tau,b}(r, y) \tilde{C}_{\tau,b}(r, y) dr,$$

where $N_{\tau,b} = |\mathcal{R}_{\tau,b}(r_{max})|$, $r_0 = 0$, and $r_N = r_{max}$. From the piece-wise constant property of $\tilde{p}_{\tau,b}(r, y)$ and $\tilde{C}_{\tau,b}(r, y)$ over the interval $(r_{n-1}, r_n]$, one can easily obtain:

$$\begin{aligned} & \int_{r_{n-1}}^{r_n} \tilde{p}_{\tau,b}(r, y) \tilde{C}_{\tau,b}(r, y) dr \\ &= \tilde{p}_{\tau,b}(r_n, y) \tilde{C}_{\tau,b}(r_n, y) \gamma(n) = p_{\tau,b}(n, y) C_{\tau,b}(n, y), \end{aligned} \quad (28)$$

where $p_{\tau,b}(n, y)$ and $C_{\tau,b}(n, y)$ are defined in the statement of Prop. 2. Therefore, substituting y with k and plugging the integration result into (26) yields the lower bound for the mutual information between map \mathbf{m} and observations $\mathcal{Z}_{t+1:t+T}$ as in (13). \square

Appendix C Proof of Prop. 3

Consider a single beam $\mathbf{z}_{\tau,b}$, passing through cells $\{m_i\}_i$, $i \in \mathcal{R}_{\tau,b}(r_{max})$. As shown in Appendix B, the mutual

information between the map \mathbf{m} and a beam $\mathbf{z}_{\tau,b}$ can be computed as:

$$I(\mathbf{m}; \mathbf{z}_{\tau,b} \mid \mathcal{Z}_{1:t}) = \sum_{k=1}^K \sum_{n=1}^{N_{\tau,b}} p_{\tau,b}(n, k) C_{\tau,b}(n, k). \quad (29)$$

Assuming piece-wise constant class probabilities, we have:

$$\begin{aligned} & \sum_{n=1}^{N_{\tau,b}} p_{\tau,b}(n, k) C_{\tau,b}(n, k) = \\ & \quad \sum_{q=1}^{Q_{\tau,b}} \sum_{n=\omega_{\tau,b,1:q-1}+1}^{\omega_{\tau,b,1:q}} p_{\tau,b}(n, k) C_{\tau,b}(n, k), \end{aligned} \quad (30)$$

where $\omega_{\tau,b,1:q} = \sum_{j=1}^q \omega_{\tau,b,j}$. For each $\omega_{\tau,b,1:q-1} < n \leq \omega_{\tau,b,1:q}$, we can express the terms $p_{\tau,b}(n, k)$ and $C_{\tau,b}(n, k)$ as follows:

$$\begin{aligned} p_{\tau,b}(n, k) &= \pi_t(q, k) \times \\ & \quad \pi_t^{(n-1-\omega_{\tau,b,1:q-1})}(q, 0) \prod_{j=1}^{q-1} \pi_t^{\omega_{\tau,b,j}}(j, 0), \end{aligned} \quad (31)$$

$$\begin{aligned} C_{\tau,b}(n, k) &= f(\phi^+ + \mathbf{E}_{k+1} \psi^+ - \chi_{0,q}, \chi_{t,q}) + \\ & \quad (n - 1 - \omega_{\tau,b,1:q-1}) f(\phi^- - \chi_{0,q}, \chi_{t,q}) + \\ & \quad \sum_{j=1}^{q-1} \omega_{\tau,b,j} f(\phi^- - \chi_{0,j}, \chi_{t,j}). \end{aligned} \quad (32)$$

Plugging (31) and (32) into the inner summation of (30) leads to:

$$\begin{aligned} & \sum_{n=\omega_{\tau,b,1:q-1}+1}^{\omega_{\tau,b,1:q}} p_{\tau,b}(n, k) C_{\tau,b}(n, k) = \\ & \quad \beta_{\tau,b}(q, k) \left[\beta_{\tau,b}(q, k) \sum_{j=0}^{\omega_{\tau,b,q}-1} \pi_t^j(q, 0) + \right. \\ & \quad \left. f(\phi^- - \chi_{0,q}, \chi_{t,q}) \sum_{j=0}^{\omega_{\tau,b,q}-1} j \pi_t^j(q, 0) \right], \end{aligned} \quad (33)$$

The summations in Eq. (33) can be explicitly computed, leading to the following closed form expression:

$$\begin{aligned} & \beta_{\tau,b}(q, k) \sum_{j=0}^{\omega_{\tau,b,q}-1} \pi_t^j(q, 0) + \\ & \quad f(\phi^- - \chi_{0,q}, \chi_{t,q}) \sum_{j=0}^{\omega_{\tau,b,q}-1} j \pi_t^j(q, 0) = \\ & \quad \beta_{\tau,b}(q, k) \frac{1 - \pi_t^{\omega_{\tau,b,q}}(q, 0)}{1 - \pi_t(q, 0)} + \\ & \quad f(\phi^- - \chi_{0,q}, \chi_{t,q}) \left[(\omega_{\tau,b,q} - 1) \pi_t^{\omega_{\tau,b,q}+1}(q, 0) \right. \\ & \quad \left. - \omega_{\tau,b,q} \pi_t^{\omega_{\tau,b,q}}(q, 0) + \pi_t(q, 0) \right] = \Theta_{\tau,b}(q, k) \end{aligned} \quad (34)$$

Therefore, the Shannon mutual information between a semantic OctoMap \mathbf{m} and a ray $\mathbf{z}_{\tau,b}$ can be computed as in (15). \square